Stowage Analysis of a Flat Flexure Elastic Hinge for Deployable Space Structures

B. Yasara Dharmadasa*
University of Colorado, Boulder 80303, Colorado
Juan Mejia-Ariza,† Jonathan Sauder,‡ Paolo Focardi,§ and Samuel Case Bradford¶
Jet Propulsion Laboratory, California Institute of Technology, Pasadena 91109, California
Manan Arya**
Stanford University, Stanford 94305, California
and
Francisco López Jiménez††
University of Colorado, Boulder 80303, Colorado

https://doi.org/10.2514/1.J064266

This paper introduces a design framework for elastically deformable hinges consisting of two parallel flat flexures, focusing on the case where the hinge is folded by 180 deg in the stowed configuration. The authors first consider architectures in which the flexures are staggered to avoid contact so that they can be modeled independently using Euler's elastica. They next focus on the nonstaggered case when folding can result in contact between the flexures, which they study through finite element simulations. The paper provides a set of design guidelines by rationalizing the relationship between hinge dimensions and the allowable curvature in the flexure material. For most hinge geometries applicable to deployable structures, the authors find a simple requirement for the minimum flexure length as a function of the allowable curvature in the material, $L_h > 10.7/\kappa_m$. Their analysis also provides insight into the reaction forces necessary to keep the hinge in the folded configuration, which is useful in determining the deployment dynamics and the constraints necessary to secure the panel in place during stowage. Experimental prototypes show good agreement with the numerical predictions.

I. Introduction

SPACE structures often require the deployment of different components, such as solar panels and antennas, due to the volume constraints imposed by the launch vehicle [1,2]. Several designs make use of flexible structural elements that can be folded elastically during storage and then deployed by releasing the stored strain energy without the need for external actuation. Inspired by the carpenter tape [3], they often consist of thin shells with curved cross-sections [4], see Fig. 1a, which can be coiled compactly in the longitudinal direction after the cross-section is flattened. When these structures are designed so that curvature is highly localized in a relatively small region [5–7], see Figs. 1b–1d, these flexures act as elastic hinges, serving the same function as mechanical hinges [8,9] while potentially reducing complexity and weight.

Elastic flexure hinges for deployable space structures need to satisfy three main requirements. First, they need to achieve the stowed configuration without exceeding the elastic strain limit of the material [10], which is a significant deviation from flexures used in complaint mechanisms that typically undergo limited rotations [11–13]. Second, they need to provide a smooth deployment path that does not damage the payload or significantly disturb the attitude dynamics of the spacecraft. Finally, they must achieve a sufficiently high natural frequency in the deployed configuration to avoid possible resonance. These three requirements often drive the design in opposite directions. For example, increasing the slenderness of the hinge elements enables higher packaging ratios during stowage but decreases the deployed natural frequency.

Most of the published studies on flexure hinges focus on the deployment process, either by characterizing the moment-curvature relationship under static loading or through dynamic experiments, including the effect of inertia and damping [5,14–18]. In contrast, relatively few studies have systematically explored the balance between designs favoring compaction during stowage and those favoring stiffness after deployment. The influence of geometry and material properties is often studied through numerical simulations [19–23] which only consider a small variation to the initial design [24] with results that are hard to generalize.

In contrast, this study is part of an attempt by us to rationalize the interplay of material and geometric parameters in elastic hinges. We focus on the case of parallel flat flexures for three reasons. First, flat flexures are a reasonable yet still complex first step in characterizing the design space, as there are fewer varying geometric parameters. Second, this analysis still provides insight into the more complex case of curved shells, once they are flattened. Previous work by us on the deployed dynamics of the flat flexure hinge [25] has already been extended to curved shells with excellent numerical and experimental agreement [26]. Finally, the flat flexure hinge may have the potential to fulfill the stiffness and compaction requirements, particularly for small-scale applications like CubeSats [27], where manufacturing ease and precision are also important. This manuscript focuses on the requirements imposed by the need for the flexure to safely fold during stowage and can be seen as a companion to the previous study that characterized the dynamics of the deployed hinge [25]. Combining the results from both studies helps guide a preliminary design to best satisfy the opposing set of requirements.

Presented as Paper 2022-0651 at the AIAA SciTech, San Diego, CA, January 3–7, 2022; received 4 April 2024; revision received 19 August 2024; accepted for publication 20 August 2024; published online 17 September 2024.

*Graduate Student, Ann and H.J. Smead Department of Aerospace Engineering Sciences. Student Member AIAA.
†Technologist, Materials Development, Testing and Failure Investigations Group. Senior Member AIAA.
‡Mechatronics Engineer, Technology Infusion Group. Senior Member AIAA.
§Group Lead for Technology Development, Spacecraft Antennas Group.
¶Supervisor, Advanced Deployable Structures. Associate Fellow AIAA.
**Assistant Professor, Department of Aeronautics and Astronautics. Senior Member AIAA.
††Assistant Professor, Ann and H.J. Smead Department of Aerospace Engineering Sciences; Francisco.LopezJimenez@colorado.edu. Senior Member AIAA (Corresponding Author).

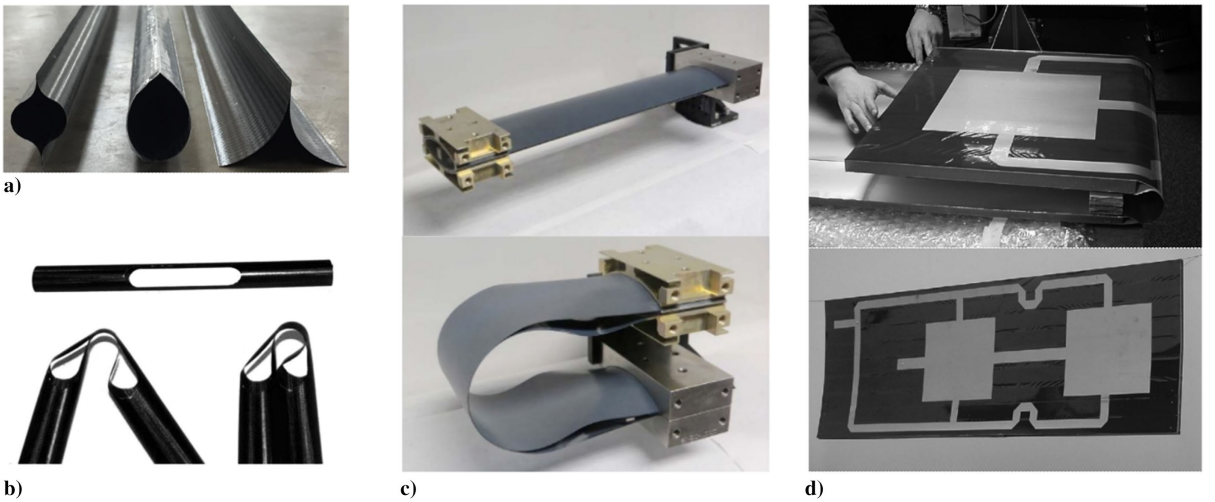

Fig. 1 Examples of HSC flexure geometries for space structures: a) coilable booms [4] and b) tape spring hinge [5]. Applications in c) high precision deployment [6] and d) large antenna design [7].

The paper is organized as follows. Section II explains the hinge design in detail, defining the geometric parameters to be explored. Section III explains the analytical and numerical framework used to characterize the folded geometry and the strain on the flexures for both noncontact and contact cases. Section IV carries out a detailed discussion of the analysis results and verifies the accuracy with prototype comparisons. Finally, Sec. V concludes this paper with a discussion of how these results could be used and possible future extensions.

II. Flat-Flexure Hinge Design

This section explains the proposed hinge design, which complements the lightweight sandwich panel architecture commonly used for space structures. The panels need to retain symmetry in the thickness direction to prevent warping or bending due to thermal stresses. Hence, functional layers are attached to either side of the panel. Examples of functional layers include reflective panels, solar panels, or electronic panels for antennas. The flat-flexure hinges can conveniently integrate with the panel by placing high-strain composite (HSC) strips at the interface between the structural and functional layer; see Fig. 2. The simplistic nature of the hinge integration omits the need for an intermediate metal bracket, improving the thermal stability of the system and easing the scalability for hinge integration. Two different folded configurations can be obtained depending on how the two flexures are placed. If the two flexures are staggered in the width direction, see

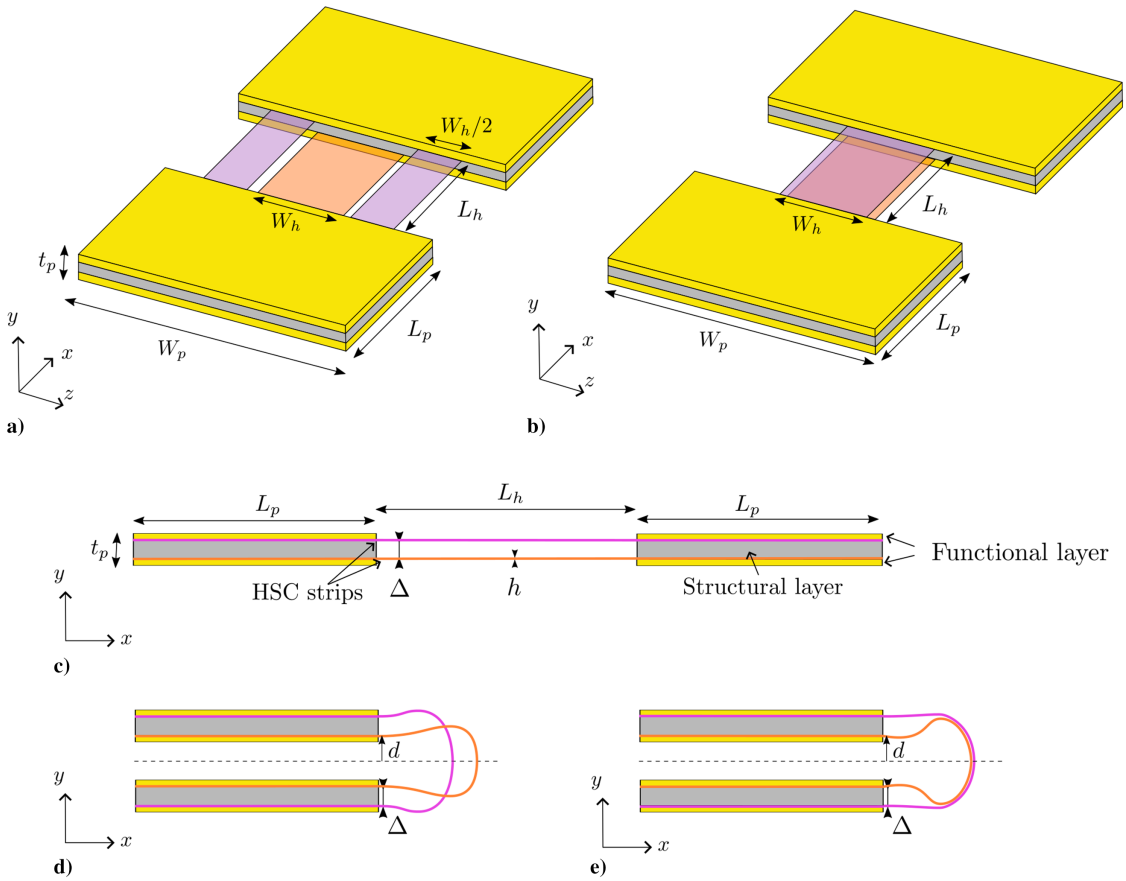

Fig. 2 Perspective views of a) staggered and b) nonstaggered hinge design, c) side view showing the flexure integration to the panel, and d,e) the folded cross-sections.

Figs. 2a and 2d, there will be no contact between the two flexures when folded. On the other hand, when flexures are not staggered, folded flexures can come into contact with each other, as illustrated in Figs. 2b and 2e. A nonstaggered flexure design can double the hinge width compared to the staggered design, increasing the overall stiffness of the hinge. In both cases, the sandwiched HSC layers are continued inside the panel to maintain a uniform panel thickness t_p. Previous work by us [25] focused on the deployed configuration, deriving closed-form relations for the natural frequency of the hinge-panel system. The proceeding sections will explore frameworks to evaluate the compaction criteria.

To understand the mechanics of folding a flat-flexure hinge, we consider two identical panels of length L_p and width W_p. The panels are connected using two flat flexures that are Δ apart, having a length L_h, width W_h, and thickness h. Folding one panel by 180 deg results in a symmetric plane parallel to x–z plane marked by the dashed line in Figs. 2d and 2e. The compaction level is parameterized by d measured from the symmetry plane to the inner flexure. We can observe the outer flexure is $d + \Delta$ away from the symmetry plane. The panels need to be stacked on top of each other for optimum packaging. If two neighboring panels are folded on top of each other (linear z folding), d is set to be the thickness of the functional layer. In other cases, such as a three-dimensional array of panels, d needs to be adjusted based on the number of panels stacked between a flexure hinge.

When folded, flat HSC flexures undergo inextensible bending, that is, zero strain at the neutral axis, and only result in curvatures in κ_z direction. The curvature profile is uniform along the z direction, and therefore only a unit width ($W_h = 1$) is analyzed using one-dimensional beam elements. The beam stiffness is estimated, $D = D_{11}$, from the ABD matrix for a given HSC laminate using conventional laminate theory. This analysis neglects the contribution of shear and out-of-plane stresses and is only intended as a first-estimate design guideline.

III. Geometric Analysis on Folded State

We will first consider the case of staggered flexures, which can be modeled as two independent flexures because they do not interact with each other and can be solved with an analytical formulation based on Euler's elastica [28]. We then use finite element simulations to study the case of nonstaggered flexures when contact is essential and compare the results to those of the staggered architecture.

A. Elastica Analysis for Folding Without Contact

We start by using Euler's elastica to model a single flexure, which is idealized as a slender element undergoing small strains but large deflections. Leveraging the symmetry in the problem, it is sufficient to model only half of the flexure $L_h/2$; see Fig. 3. The curvilinear coordinate s measured from the panel base parameterizes the beam profile. The deformed shape is expressed using the local angle profile: $\theta(s) = -(dy/dx)(s)$. We assume the panel remains horizontal in the compacted state, providing the boundary condition $\theta(0) = 0$. The vertical position Y_0 indicates the level of compaction, which in the stowed configuration will equal d (for the innermost flexure) or $d + \Delta$ (for the outermost flexure). The symmetry of the system imposes $\theta(L_h/2) = \pi/2$ and zero horizontal reaction forces. The beam is subjected to a vertical force F at the supports, fixed end moment M_1 at the panel, and M_2 at the symmetry line. The folding

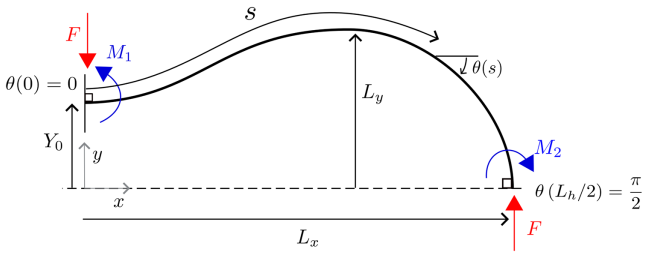

Fig. 3 Schematic of elastica problem for the HSC strip bending, including lengths and reaction forces.

results in maximum projection lengths L_x and L_y in the horizontal and vertical directions, respectively.

Equilibrium of moments provides a relationship between the boundary conditions:

$$M_2 = FL_x + M_1 \tag{1}$$

The moment at any arbitrary point s along the beam is

$$M(s) = M_1 + Fx(s) \tag{2}$$

The problem can be solved using the elastica equations to integrate the angle

$$\theta(s) = \int_0^s \kappa(\xi)\,\mathrm{d}\xi = \int_0^s \frac{M(\xi)}{D}\,\mathrm{d}\xi \tag{3}$$

with initial condition $\theta(0) = 0$. Here, ξ is the integration variable, and κ is the local curvature. The $x(s)$ and $y(s)$ coordinates can be obtained by integrating the local angle,

$$x(s) = \int_0^s \cos\theta(\xi)\,\mathrm{d}\xi \tag{4}$$

$$y(s) = \int_0^s \sin\theta(\xi)\,\mathrm{d}\xi + Y_0 \tag{5}$$

subjected to boundary conditions $x(0) = 0$ and $y(0) = Y_0$. In addition, the flexure must satisfy the boundary condition $\theta(L_h/2) = \pi/2$ and $y(L_h/2) = 0$. These boundary conditions are satisfied through a shooting algorithm that guesses the value of F and M_1.

The problem can be transformed into a nondimensional form by scaling the lengths with $L_h/2$ and the forces and moments with the bending stiffness D; see Eqs. (6–9). Nondimensional parameters are marked with a hat; for example, $\hat{M}$ is the nondimensional form of the bending moment M:

$$\hat{s} = \frac{s}{(L_h/2)} \tag{6}$$

$$\hat{F} = \frac{F(L_h/2)^2}{D} \tag{7}$$

$$\hat{M} = \frac{M(L_h/2)}{D} \tag{8}$$

$$\hat{\kappa} = \kappa(L_h/2) \tag{9}$$

A MATLAB® script using the numerical integrator ode45 is used to solve the set of coupled differential equations [Eqs. (3–5)]. Figure 4 illustrates the geometric profiles obtained for various $\hat{Y}_0$ values. Note

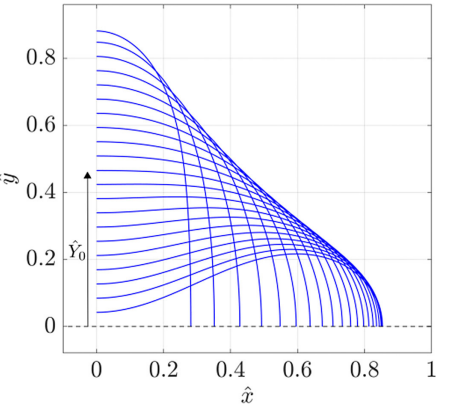

Fig. 4 Beam profiles obtained by solving the elastica equations.

that the profiles are dimensionless; therefore, the results (geometry, forces, and moments) can be scaled using the corresponding length and stiffness values.

B. Finite Element Analysis for Folding with Contact

Next, we performed a series of finite element simulations using the commercial software package ABAQUS to model the nonstaggered case where the two flexures can come into contact when folded. The same assumptions from the previous elastica analysis are carried forward; only half the flexure is modeled due to symmetry. The problem can be modeled with beam elements (B21) of thickness h having isotropic material properties (E_0 and ν). The beams are assembled at a distance Δ apart from each other, and a Multi-point constraint (MPC) is used to tie the edge nodes to a reference point to maintain the constant spacing and angle throughout the analysis; see Fig 5a. Note that the translation and rotation degrees of freedom are tied to the reference point. The opposite edges of the beams are assigned with symmetric boundary conditions (no displacement in the vertical direction and no rotation). *Hard* and *frictionless* contact is defined between the two beams. The analysis is carried out in two stages: first, obtaining the folded configuration and then varying the compaction level. In the first step, the reference point is rotated by $\pi/2$ and translated by a desired amount to achieve the folded state $d = 0$; see Fig. 5b. Next, the reference point is translated while maintaining the same boundary angle to achieve different $d - \Delta$ configurations. Rigid-body motions are constrained by fixing the horizontal displacement of the reference point. Figure 5 illustrates the case when $L_h/2 = 10$ mm, $\Delta = 1$ mm. Taking inspiration from the elastica analysis, the results are nondimensionalized using $L_h/2$ and $D = E_0 h^3/(12(1-\nu^2))$.

C. Hinge Prototype

The analytical and finite element (FE) models of the folding hinge are based on several assumptions, such as zero flexure thickness, no friction when in contact, perfectly flat flexures, and perfect alignment during fabrication. In reality, all these assumptions might not hold true. To assess the validity of the mentioned analysis, a simple prototype of the hinge is made using acrylic plates and HSC strips. Three different thicknesses of acrylic plates are used: 1.5, 3.0, and 6.0 mm (to aid visualization, plates will appear clear, colored red, and green, respectively), with different stacking orders to create a range of $d - \Delta$ values. The HSC strips are made of a single ply of carbon fiber prepregs (T300-1k plain-weave fibers with EX1515 epoxy) having a thickness of $h = 0.12$ mm. The strips are cut with fibers directed at ± 45 deg with respect to the hinge direction and the strip width is set at $W_h = 25.4$ mm. Flexures are aligned and attached to the acrylic plates using adhesive tapes in the unfolded state and then folded and secured using four bolts on the plate edges; see Fig. 6.

IV. Results and Discussion

A. Nondimensional Elastica Analysis

In this section, we first explore the findings from the generalized elastica analysis, which can be applied to the staggered two-flexure hinge by reintroducing parameters $\hat{Y}_{0,\text{inner}} = \hat{d}$ and $\hat{Y}_{0,\text{outer}} = \hat{d} + \hat{\Delta}$.

First, we investigate the stowed volume requirement of the elastically deformable hinge, which is of critical importance for a deployable satellite. As illustrated in Fig. 3, the folded hinge needs a minimum clearance of L_x and $2L_y$ in horizontal and vertical directions, respectively. The dimensionless dependence of these clearances as a function of the compaction level $\hat{Y}_0$ is plotted in

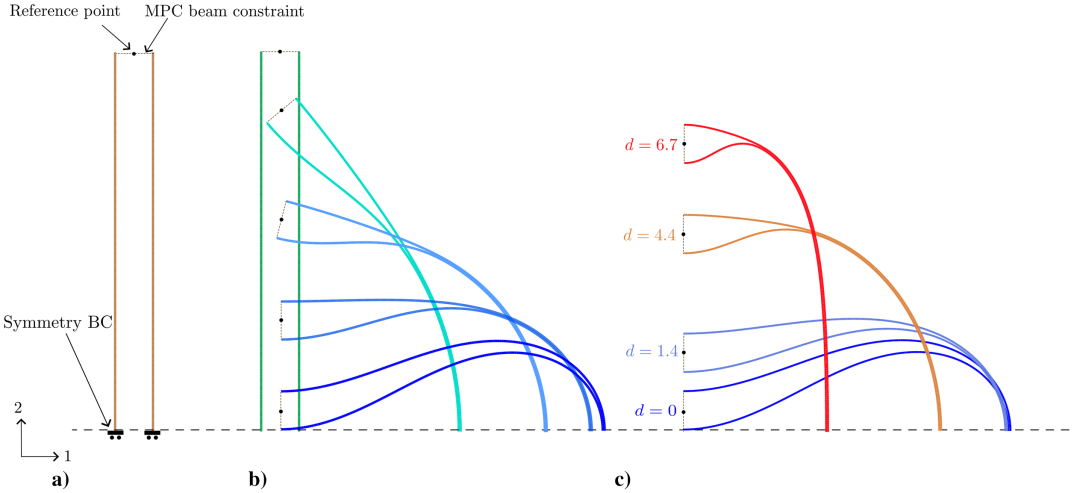

Fig. 5 FE modeling of non-staggered flexures. a) initial configuration, b) folding to $\theta = 0$ and $d = 0$, c) increasing d at $\theta = 0$.

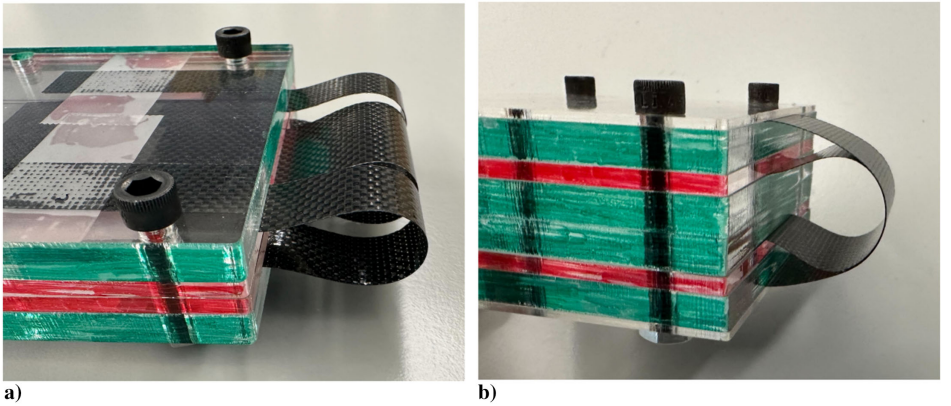

Fig. 6 Hinge prototype made out of acrylic plates and HSC flexures: a) staggered design and b) nonstaggered design.

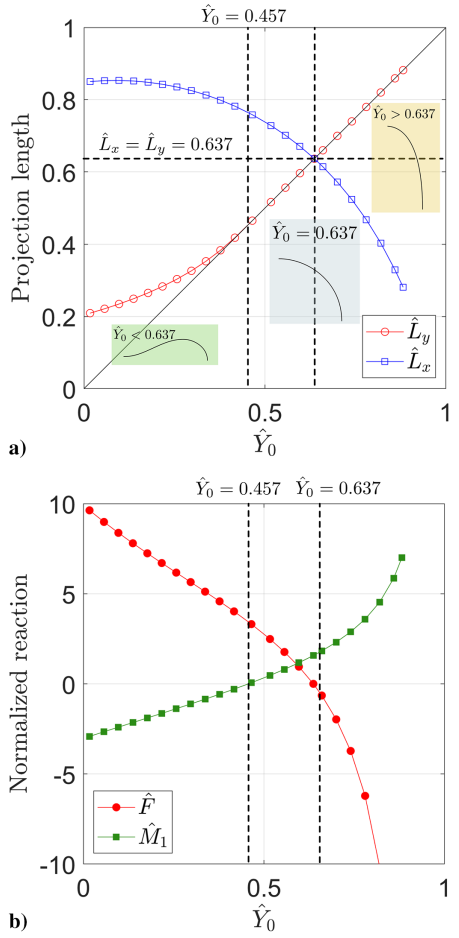

Fig. 7 Elastica results for different compaction levels: a) horizontal and vertical projection and b) normalized forces and moments.

Fig. 7a. If the minimum clearance is not met, undesirable deformations can occur, triggering flexure failure. We observe a maximum horizontal projection around 0.85 times the beam length at high compaction level $\hat{Y}_0 = 0.1$, which gradually drops to less than 0.3 times the beam length when $\hat{Y}_0 \approx 0.9$. On the other hand, we observe a low vertical projection around $\hat{L}_y \approx 0.2$ at high compaction, which increases with $\hat{Y}_0$. When $\hat{Y}_0 > 0.457$, the vertical projection is equal to the compaction ($\hat{L}_y = \hat{Y}_0$), the highest extrusion point is at the panel boundary $s = 0$, and the flexures are contained within the panel thickness. Special care should be allocated for cases when $\hat{Y}_0 < 0.457$ because the flexures protrude out from the panel boundary. The relations have been quantified with fittings, which can be found in the Appendix.

Next, we look at the variation of reaction force $\hat{F}$ and moment $\hat{M}_1$ for each compaction level; see Fig. 7b. At low $\hat{Y}_0$ values, the flexure would need a downward force and a clockwise moment exerted through the panels. As $\hat{Y}_0$ increases, the magnitude of the force and moment decrease. At $\hat{Y}_0 \approx 0.457$, the moment becomes zero corresponding to the case of a pinned flexure purely under a compressive force. This is an important geometric configuration discussed in the vertical projection length $\hat{L}_y$. Further investigations reveal that the opposite force and moment results in negative curvatures at the base of the beam, bending it outward when $\hat{Y}_0 < 0.457$. However, the beam deforms inward after M_1 direction flips, making the highest vertical projection at the base for $\hat{Y}_0 > 0.457$. As $\hat{Y}_0$ increases, we meet the next point of interest when $\hat{F} = 0$. The flexure experiences a pure bending moment, constant along the arc length, resulting in a constant curvature, that is, the deformed shape is a quarter-circle. In this configuration, $\hat{Y}_0 = \hat{L}_x = \hat{L}_y$ is the radius of the quarter circle, equal to $(2/\pi) \approx 0.637$ because the arc length of the quarter-circle is $\hat{L}_h = 1$. As $\hat{Y}_0$ increases further, the reaction force becomes negative, while the reaction moment keeps increasing.

We now focus on the normalized curvature $\hat{\kappa}$ along the flexure arc length $\hat{s}$. The normalized curvatures for all possible $\hat{Y}_0$ configurations can be represented in a contour map; see Fig. 8a. For lower $\hat{Y}_0$, the base of the flexure has a negative curvature, while the symmetry point has a positive curvature. This observation is consistent with the previous discussion, where the zero-curvature contour (shown in white) represents the inflection points, and the curvature becomes positive at $\hat{Y}_0 \approx 0.457$. We track the maximum curvature values (red dashed line), which remains at the symmetry point ($\hat{s} = 1$) in $\hat{Y}_0 < (2/\pi) \approx 0.637$. Constant curvature is observed at $\hat{Y}_0 = 0.637$, where the beam has the minimum bending energy. At higher $\hat{Y}_0$, higher curvatures are observed at the beam base ($\hat{s} = 0$). Although the force becomes negative in this range, it is interesting to note that the curvatures remain positive due to the more dominant effect of the reaction moment.

Flexure failure will likely occur at the maximum curvature point, extracted onto Fig. 8b. Because this relation is unique to all geometries resulting from two flexures, we can define a maximum curvature function $G(\hat{Y}_0)$. The function $G(\hat{Y}_0)$ is fitted to a polynomial and rational function; see Appendix. Next, we apply the generalized results discussed previously to the specific case of flat flexure hinge design by considering the case of two flexures.

B. Compaction Limit of Flat Flexures

For the hinge to survive the folded state, the flexures should not undergo strains larger than the critical strain ε_{cr}. If the tensile and compressive responses are assumed to be identical, the critical strains are proportional to the critical curvature; in the case of an isotropic material, $\kappa_{cr} = 2\varepsilon_{cr}/h$, where h is the thickness of each flexure, while in a composite, $\kappa_{cr} = 2\varepsilon_{cr}/t_c$, where t_c is the distance from the neutral axis to the ply that fails first. The geometric parameters

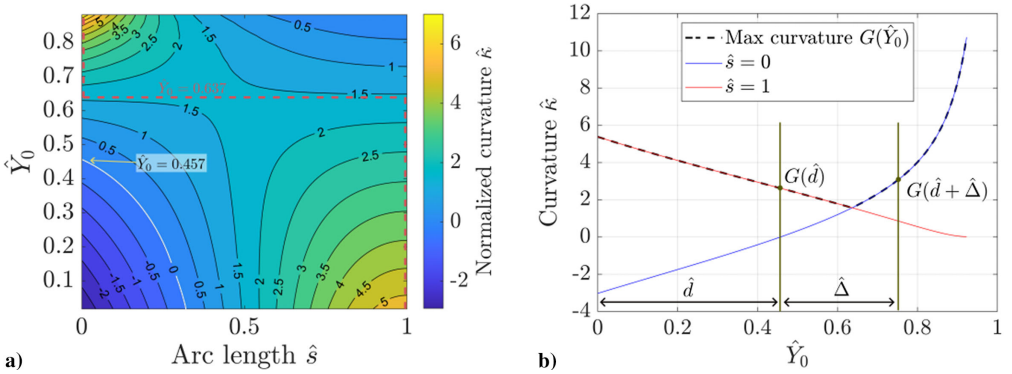

Fig. 8 Identifying critical curvatures by plotting a) normalized curvature contours along the arc length for different $\hat{Y}_0$. Maximum curvature profile is highlighted by the dashed line. b) Maximum curvature G variation for different $\hat{Y}_0$.

d, Δ, L_h and h should be selected such that the maximum curvatures are below the critical values. Note that the analysis only accounts for possible failure due to the bending of the flexure and neglects the contribution of the normal stresses due to the reaction forces. As such, it should be treated as an initial step in the design process.

Figure 8b shows the maximum curvature values for any flexure that does not undergo contact, ergo, staggered design. The two flexures will have offset values of $\hat{Y}_0 = \hat{d}$ for the inner flexure and $\hat{Y}_0 = \hat{d} + \hat{\Delta}$ for the outer flexure, as shown by the two vertical lines in Fig. 8b. The maximum curvature on the hinge will then be $\hat{\kappa}_{m,s}$, which is defined as

$$\hat{\kappa}_{m,s} = \max(G(\hat{d}), G(\hat{d} + \hat{\Delta})) \tag{10}$$

Figure 9a shows the maximum curvature on the hinge $\hat{\kappa}_{m,s}$ as a contour map based on the values of $\hat{\Delta}$ and $\hat{d}$. The global minimum for a two-flexure hinge is obtained when $\hat{\Delta} \approx 0$ (so that both flexures are basically overlapping) and $\hat{Y}_0 = 0.637$. As $\hat{\Delta}$ increases, the maximum normalized curvature depends on the corresponding $\hat{d}$ value. If $\hat{d} + \hat{\Delta} < 0.637$, the inner flexure will always have higher normalized curvature, while for $\hat{d} > 0.637$, the outer flexure will always be critical. In all other configurations, the maximum normalized curvature can occur in either flexure, and $\hat{\kappa}_{m,s}$ is minimized when $G(\hat{d}) = G(\hat{d} + \hat{\Delta})$. The relation also indicates the critical location of maximum strain, which is either the point of connection to the panel (for $\hat{Y}_0 < 0.637$) or the midpoint (for $\hat{Y}_0 > 0.637$). This information is useful during fabrication to reinforce or focus fabrication precision on critical points.

Next, we consider designs where the flexures are in contact. A series of finite element simulations are performed, with $L_h/2 = 10$ mm, $h = 0.1$ mm, $E_0 = 10^6$ MPa, and $\nu = 0.3$ (note that the value of the stiffness is not important because we are scaling the forces/moments with the corresponding D). We vary the panel separation Δ using 30 equidistant points between 0 and 5 mm, meaning $0 \le \hat{\Delta} \le 0.5$ in nondimensional form. For each Δ configuration, d values are varied between $[0, (0.8 - \Delta)]$ at 100 equidistant points. All extracted data are nondimensionalized following Eqs. (6–9). A similar concave curvature map is observed when the flexures are in contact $\hat{\kappa}_{m,ns}$, but with a nonlinear dependence on the $\hat{\Delta}$ axis and a drastic curvature increase at high $\hat{d} - \hat{\Delta}$ combinations.

Comparing the normalized contour maps for noncontact and contact hinges, we identify regions that result in the lowest curvature, and hence the strain, depending on the specific combination of $\hat{d} - \hat{\Delta}$ values. To highlight the comparison, we plot the ratio between the maximum curvature on each case $\hat{\kappa}_{m,ns}/\hat{\kappa}_{m,s}$ in Fig. 10a. When the curvature ratios are larger than one, nonstaggered design results in higher curvatures compared to staggered design and vice versa. To provide further insight into this behavior, we investigate several point cases plotting the deformed geometry and the curvature distribution for nonstaggered (blue) and staggered (red) designs; see Figs. 10b–10f (inner flexures are solid lines, and outer flexures are dashed lines). In the staggered case where no contact occurs, the highest curvature is recorded at either $\hat{s} = 0$ (the attachment to the panel) or $\hat{s} = 1$ (the symmetry point). In contrast, geometric constraints are imposed on the two flexures to share the same curvature profile when they are in contact, modifying both deformed profiles. As a result, the highest curvature can take place at any point of the arc length.

We first consider cases with high $\hat{d}$ values, where contact between the flexures results in significantly higher curvatures, up to three times that of the noncontact design. Figure 10b shows that the inner flexure needs to bend tightly to fit inside the envelope of the outer flexure, and high curvatures are observed between the base and the point where contact between the flexures begins. The curvatures are significantly lower near the center of the flexure.

We observe the opposite behavior in the next highlighted region, where the maximum curvature ratio is less than 1. In this case, the two beams are in contact for a shorter length, and therefore the inner flexure has sufficient length to smoothly reconfigure without causing major curvature changes, as shown in Figs. 10c and 10f. Additionally, contact helps to reduce the critical curvature of the inner flexure, resulting in an overall reduction of the maximum curvature of up to 20%. We observe a special case in between the two mentioned regions, where the contact changes the deformed profile but still maintains the same maximum curvature, that is, when the values of the contour plot are equal to 1. Interestingly, even if the maximum curvatures are the same for both designs, they take place at different points of the arc length; see Fig. 10d. Both designs are equally desirable from a curvature standpoint; however, a more compact folded configuration can be obtained when the flexures are in contact. This will be addressed in detail in the next section.

Another interesting feature appears at the bottom of the contour map, around $\hat{\Delta} = 0.05$–0.14 and $\hat{d} = 0$, where the curvature contour again becomes 1. As opposed to the previous case, plotting the deformed shapes reveals that, in this case, both cases have the same geometry; see Fig. 10e. In this limited parameter window, the inner flexure is contained inside the outer beam without any contact. This is the only window where nonstaggered hinges can be folded without contact between them, except for point contact at the symmetry edge. For all other $\hat{\Delta}$ or $\hat{d}$ combinations in nonstaggered design, contact in a finite region is inevitable as seen in Fig. 10f.

The mentioned analysis uses nondimensional variables, in which all lengths are scaled by L_h, providing a comprehensive study of all possible geometries. However, the design of a hinge is often driven by a priori knowledge of the values of Δ (given by the thickness of the panels) and κ_m (given by the failure properties of the flexure material), with the other parameters to be decided based on the analysis. Exploring the effect of changing L_h and d in Figs. 9 and 10 can be complex, as it changes both axis values and the contour values. Hence, we replot the same data in Figs. 11a and 11b by changing the normalization parameter to Δ. The maximum curvature contours $1/\kappa_m\Delta$ are plotted as a function of the level of compaction d/Δ and minimum flexure length L_h/Δ. To increase the clarity of the contour map, the horizontal axis has been plotted in logarithmic scale for $d/\Delta < 5$. Both cases (contact and noncontact) show a similar behavior with slight changes in the contour values, which is visualized in Fig. 11c.

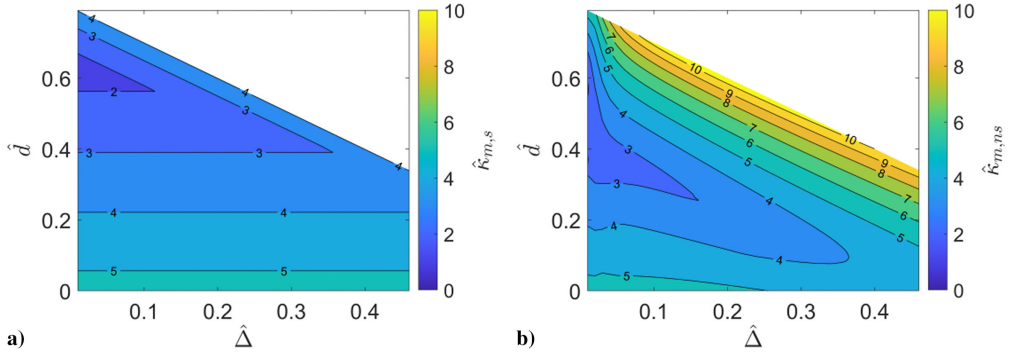

Fig. 9 Maximum normalized curvature contours as a function of $\hat{d}$ and Δ for a) staggered and b) nonstaggered flexure hinges.

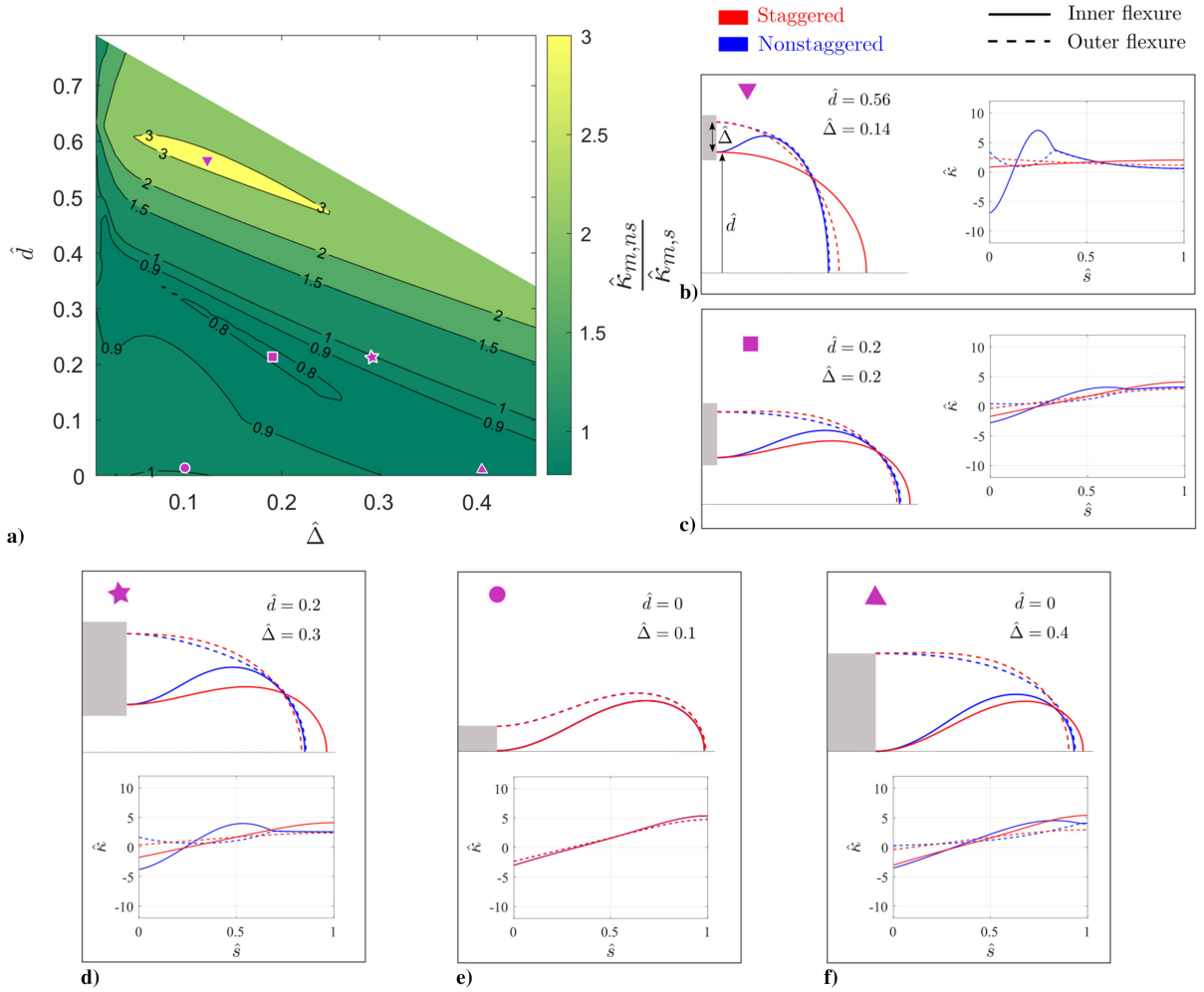

Fig. 10 Comparing the compaction limit for staggered and non-staggered hinges. a) Visualizes maximum curvature ratios and b–f) plots the deformed profiles and the curvature distributions for point cases shown in a.

The dependence of the flexure length L_h on the distance between panels in the stowed configuration d can be understood by following the path of the contour lines of constant nondimensional maximum curvature $1/\kappa_m\Delta$ in Fig. 11. When the stowed configuration is very compact, that is, $d/\Delta \approx 0$, the minimum hinge length that provides constant curvatures is approximately constant, $L_h \approx L_h^0$; that is, the contour lines are approximately horizontal. As d increases, the required flexure length reaches a minimum value $L_h^* \approx L_h^0/2$ at d^*. Further increasing d results in an increase of L_h, with all contour lines converging. Setting the hinge design at d^*, L_h^* results in the shorter flexure for a given combination of panel thickness and material failure $\kappa_m\Delta$. This can be considered the optimum design point if the goal is to increase the natural frequency of the first resonance mode when the structure is deployed [25]. It should be noted that these optimum points correspond to the case $G(\hat{d}) = G(\hat{d} + \hat{\Delta})$, discussed previously.

The optimum design parameters L^* and d^* are shown in Figs. 12a and 12b with linear fittings. Overall, noncontact flexures can provide the shortest hinges. It is interesting to note that both noncontact and contact hinges have the same length requirement at low compaction levels (L_h^0). Neglecting the zone $d > d^*$ where curvatures drastically increase, we can provide a general length requirement for the flexures to safely fold without failing in bending as

$$L_h \geq \frac{10.70}{\kappa_m} \tag{11}$$

C. Stowed Hinge Clearances

Next, we move on to the dimensions of the flexures in the stowed configuration, which are quantified by the two lengths $\hat{L}_x$ and $\hat{L}_y$. Figures 13a and 13b plots the dependence of $\hat{L}_x$ and $\hat{L}_y$ for noncontact flexures, and Figs. 13c and 13d plots that for contacting flexures, as $\hat{d}$–$\hat{\Delta}$ parameters are varied. For the noncontact case, the horizontal distance is only dependent on $\hat{d}$, suggesting it is dominated by the inner flexure. Contact between the flexures shortens the overall horizontal projection around by 10–40%, depending on the region; see Fig 13e. The vertical projection is dependent on both $\hat{d}$ and $\hat{\Delta}$. Contact between the flexures helps reduce $\hat{L}_y$ for all cases except for low $\hat{\Delta}$ and $0.1 < \hat{d} < 0.4$; see Fig. 13f. These plots provide design guidelines that can be used to choose geometry based on the required geometry constraints during stowage.

D. Experimental Demonstration

Several design cases were replicated using prototypes to validate the numerical results obtained before. Table 1 indicates the different geometries explored and the expected maximum curvatures from Fig. 11.

Self-similarity of the geometry is used throughout this analysis, which is first verified through the prototypes. We consider two designs with the same $\hat{\Delta} = 0.1$ and $\hat{d} = 0$, but the values of L_h and Δ differ by a factor of 2; see Fig. 14. When the deformed profiles are scaled by L_h and overlayed on top of each other, we observe the same geometry, verifying the scalability of the results.

We now consider six different point case designs and compare the deformed shapes against predicted geometries from the analysis. In all the cases, hinge length is set at $L_h = 60$ mm. Figure 15 shows pictures of the stowed configuration for the six designs, with the predicted shape overlayed. In all cases, we observe excellent agreement between the shape of the flexures in the prototypes and our predictions.

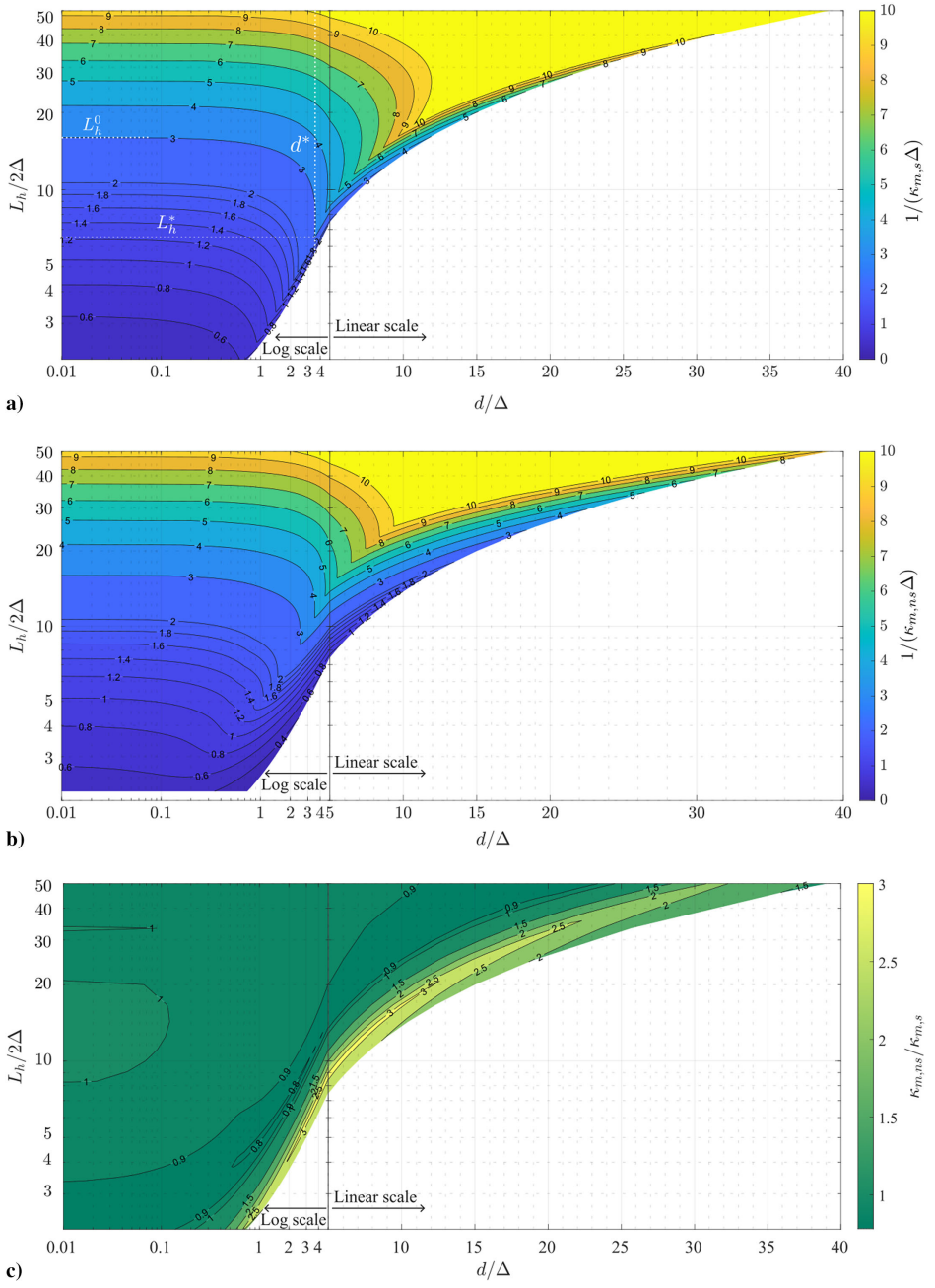

Fig. 11 κ_m curvature contours for L_h and d variation for a) staggered and b) nonstaggered flexures. L_h^0, L_h^*, and d^* are shown for $1/(\kappa_{m,s}\Delta) = 3$ contour. c) Contour ratios from parts a and b.

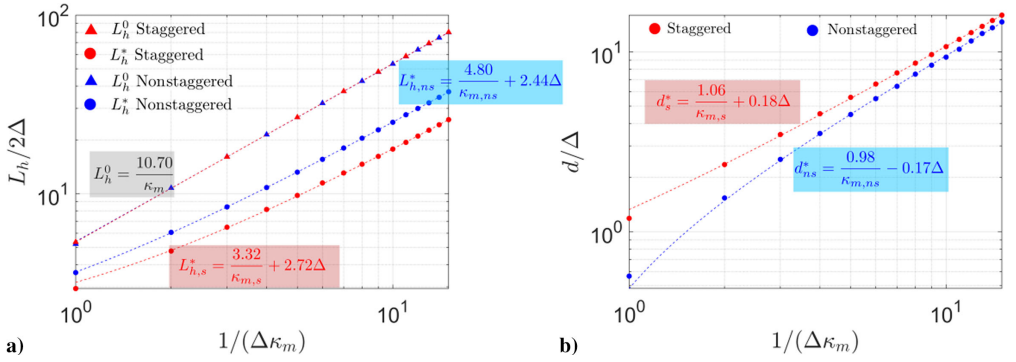

Fig. 12 a) minimum length requirements L_h^0 and L_h^* and b) corresponding compaction level d^* for each curvature level.

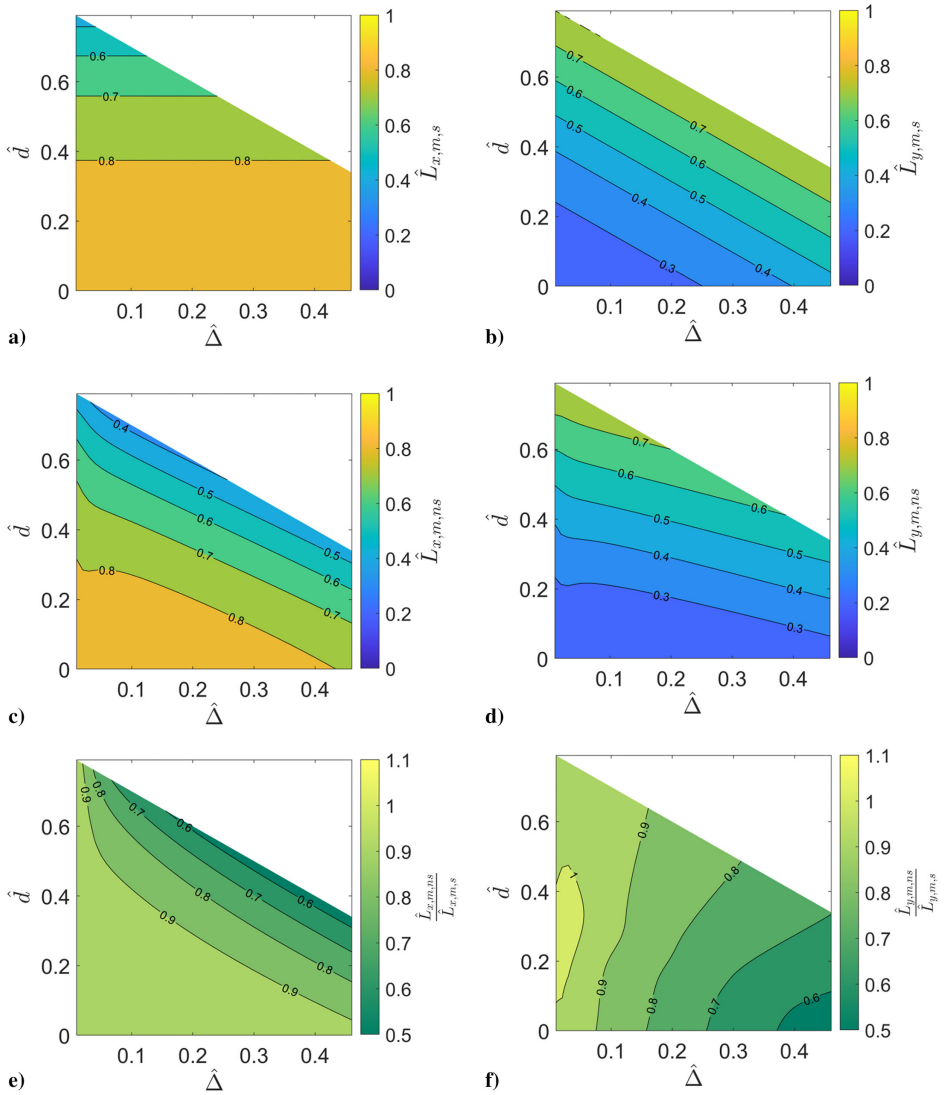

Fig. 13 Contour plots of $\hat{L}_x$ (left) and $\hat{L}_y$ (right) as a function of $\hat{\Delta}$ and $\hat{d}$ for a,b) staggered, c,d) nonstaggered, and e,f) ratio between the two cases.

Table 1 Design cases for the prototypes

Type	L_h, mm	Δ, mm	d, mm	$\frac{L_h}{2\Delta}$	$\frac{d}{\Delta}$	$\frac{1}{\kappa_m \Delta}$	κ_m, mm^{-1}
Noncontact	60	3.0	0	10.0	0	1.9	0.18
	60	6.0	6.0	5.0	1.0	1.2	0.14
	60	9.0	6.0	3.3	0.7	0.8	0.14
Contact	60	3.0	0	10.0	0	1.9	0.18
	60	6.0	6.0	5.0	1.0	1.5	0.11
	60	9.0	6.0	3.3	0.7	0.6	0.19
	120	3.0	0	20	0	3.8	0.09

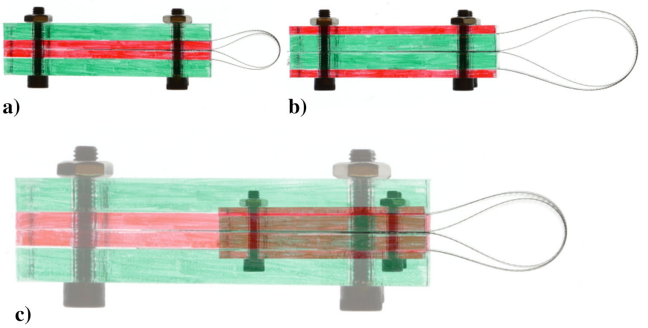

Fig. 14 Self-similarity of the geometry for two cases a) $L_h = 60.0$ mm, $\Delta = 3.0$ mm, $d = 0$; b) $L_h = 120.0$ mm, $\Delta = 6.0$ mm, $d = 0$; and c) both cases overlapped with first scaled by a factor of 2.

E. Reaction Forces and Moments on Panel

We finally use our framework to characterize the reaction forces and moments that the flexures exert on the panels, with two goals. First, these reactions are the initial conditions that need to be considered to analyze the deployment dynamics of the panels due to the stored strain energy in the flexure. Second, understanding the reactions is necessary to design the locking mechanisms that safely hold the panels during the stowed period.

Using the same symmetry assumptions, the flexures exert a force F_{panel} and a moment M_{panel} on the panel, defined as positive when in the outward and clockwise directions, respectively; see Fig. 16a. The evolution of the reactions over different geometries can be visualized by plotting contours on the same nondimensional axes as before. Note that the reaction forces and moments are also nondimensionalized following Eqs. (7) and (8). For low values of $\hat{d} - \hat{\Delta}$, both noncontact and contact hinges produce an outward reaction force, while for larger $\hat{d} - \hat{\Delta}$, the direction flips; see Figs. 7b and 7d. A similar response is observed for the reaction moments where the values are initially counterclockwise and later become clockwise; see Figs. 7c and 7e. The change in the direction of the reactions can be rationalized by considering again Fig. 7b, which shows the evolution of

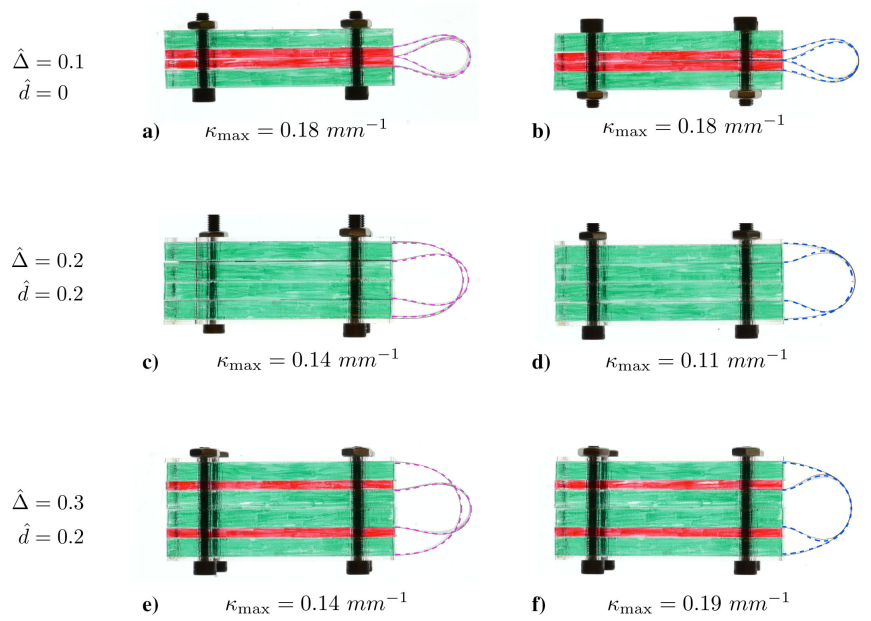

Fig. 15 Comparing the prototype geometry against the predicted shapes (dashed lines) for a,c,e) staggered and b,d,f) nonstaggered cases.

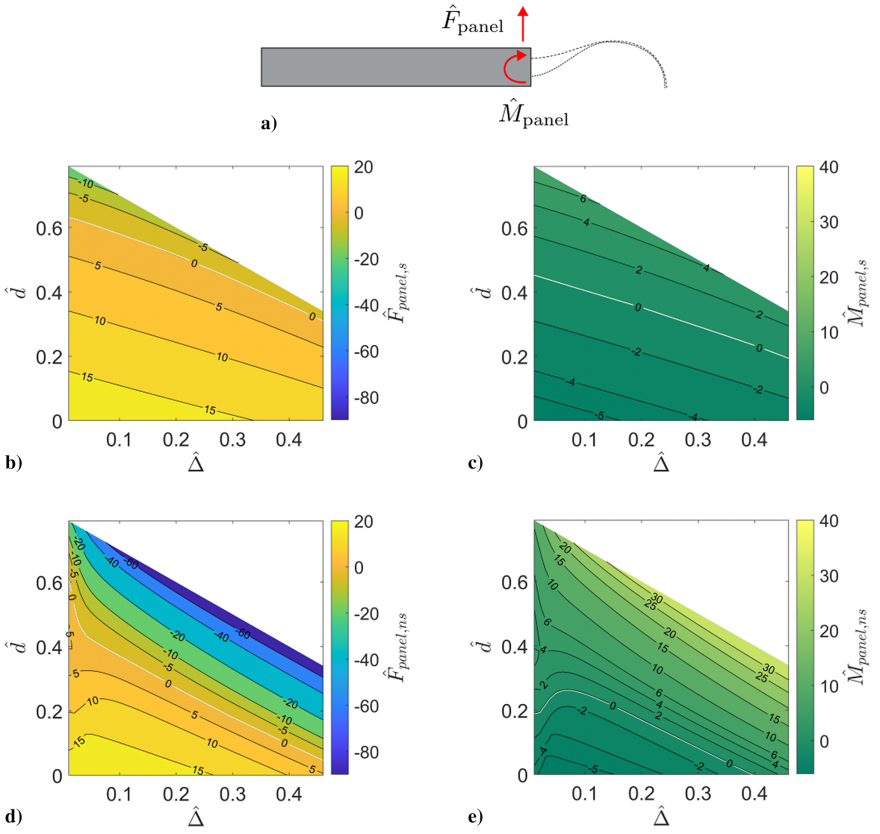

Fig. 16 Normalized reaction force and moment exerted on the panel. a) sign convention, b,c) staggered case and d,e) non-staggered case.

reaction forces and moments on a single flexure as a function of the geometry of the stowed configuration.

We can combine the information in Figs. 16b–16e to identify three distinct regions in the design space based on the changes in sign in the forces and moments. These regions are shown in Figs. 17a and 17b for the noncontact and contact cases, respectively. For both architectures, there is a region with positive force and negative moment (region C1) for low values of both $\hat{d}$ and $\hat{\Delta}$. As we move away from the origin, we transition first to a region with positive force and moment (region C3), followed by negative force and positive moment (region C5). The lines delineating these regions are different for both architectures and correspond to geometries that result in zero reaction moment (labeled as C2) and zero reaction force (labeled as C4). Figure 17c presents schematics for each case, including both the reaction forces and moments, as well as the expected direction of the initial displacement during deployment. The illustration only offers insight into the initial conditions for the dynamics, and the subsequent deployment would need to consider both the inertia of the panel and the response of the flexures as they deploy.

The initial forces and moments shown in Figs. 16 and 17 also offer insight into how to secure the panels in the folded configuration. Assuming the mirroring panel (not shown in the illustration) provides

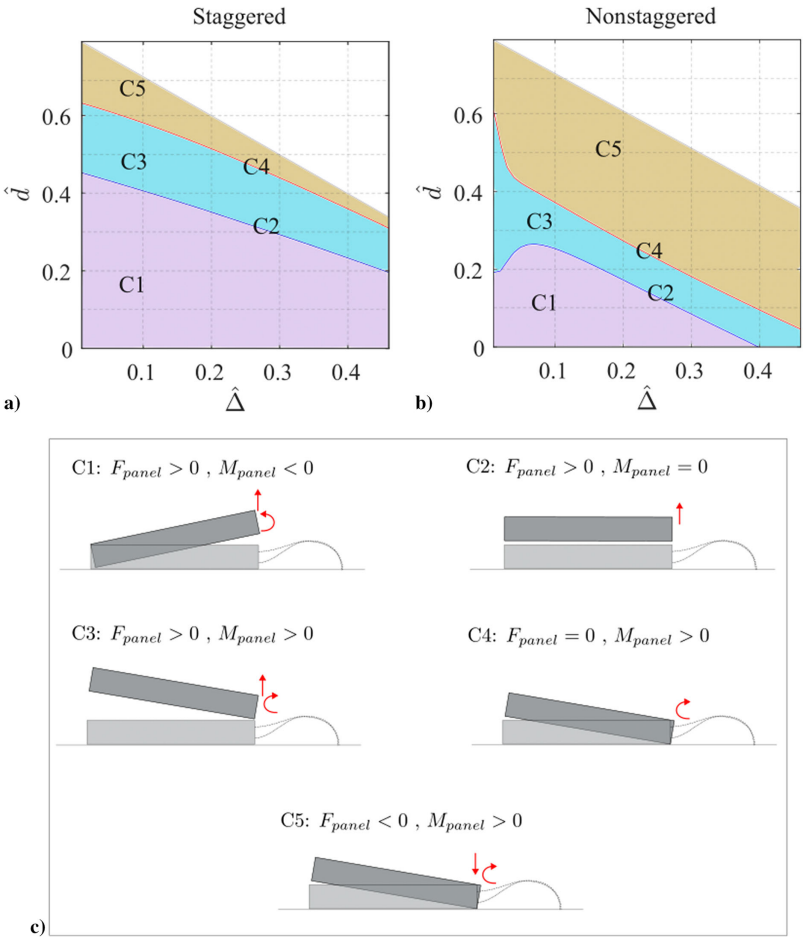

Fig. 17 Different regions where the direction of panel force and moment change for a) staggered and b) nonstaggered hinges; c–f) the initial motion in each region.

outward reaction forces through contact, cases C4 and C5 can be stably folded using a downward force exerted at the free edge of the panel. However, for regions C1, C2, and C3, the securing force needs to be applied at the base of the hinge or through multiple points.

Figure 18 further visualizes this concept, where prototypes are allowed to freely deform by a small amount from the fully folded state while being held away from the hinge. The flexure length is fixed at $L_h = 60$ mm, and Δ and d are varied to explore different regions in Fig. 17. The three samples in Figs. 18a–18c have two flexures have the two flexures in contact and, based on the $\hat{d}$–$\hat{\Delta}$ combinations, belong to C1, C3, and C5, respectively. Excellent agreement is observed between the prototypes and the predictions. The final sample, Fig. 18d, has the same geometry as Fig. 18c, but the flexures are not in contact. We observe that the response is significantly different and now belongs to C1, as predicted by the analytic model.

V. Conclusions

This paper has presented a compaction study on a simplified hinge architecture, which uses two parallel flat flexures that can smoothly

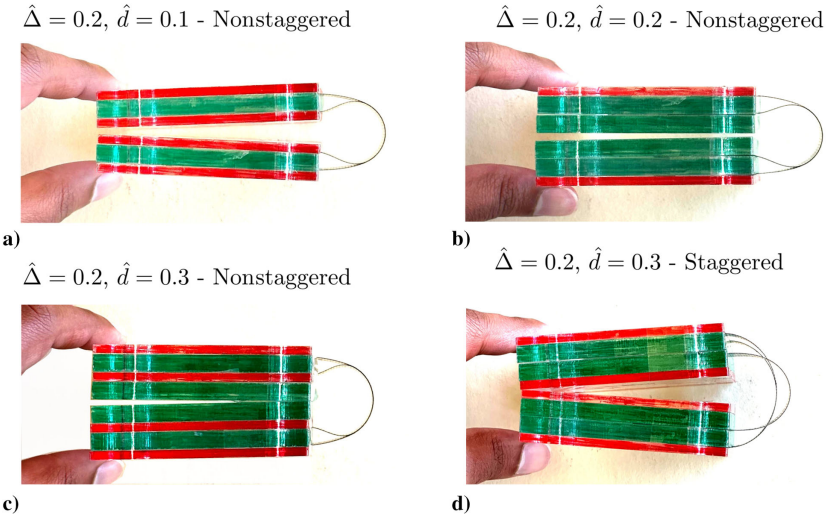

Fig. 18 Initial panel motion under a gripping force at panel end for a–c) nonstaggered and d) staggered hinges.

and easily integrate with flat panels. The authors have explored two different hinge architectures. First, they assumed the flexures are staggered along the width so that they do not contact each other when folded, and the geometry can be solved analytically using elastica theory. The analytic relations shed light on the self-similarity of the folded shapes, providing us the opportunity to explore the full design spectrum. They then considered the case of nonstaggered flexures so that they come in contact with each other in the stowed configuration. A series of finite element simulations were conducted, and the results were transformed to the same nondimensional format.

The flexures, when folded, should only undergo elastic strains without causing plastic strains or material fracture. The authors explore the variation of flexure curvatures as a function of hinge parameters and compaction levels for both noncontact and contact cases. Their results show that for low $\hat{d}$–$\hat{\Delta}$ combinations contact helps to reduce the maximum curvature, while for large $\hat{d}$–$\hat{\Delta}$ combinations, contact between the flexures increases their maximum curvature. The authors have obtained a rule of thumb for estimating the hinge length as a function of the maximum allowable curvatures, $L_h > 10.7/\kappa_m$, which is valid for most geometries of interest for deployable structures. They have also found an optimum value for the compaction level, $d = d^*$, that can reduce the length almost by half when compared to other geometries.

The authors also estimated the effect of the geometry of the system on the size of the flexures when folded, which is characterized by their projection lengths L_x and L_y. This provides an estimate of the clearance required for the hinge in the folded state. They observe that contact between the flexures helps reduce the projection lengths, resulting in a more compact stowed configuration. Finally, they studied the reaction force and moment applied on the panel by the folded flexures. At low $\hat{d}$–$\hat{\Delta}$ combinations, an outward force and a counterclockwise moment are applied on the panel for both contact and noncontact cases. As $\hat{d}$–$\hat{\Delta}$ parameters increase, the forces and moments reduce and flip in sign. The authors identify different response regions based on the direction of force and moment and show that the initial deployment dynamics may significantly vary based on the selected parameters and the presence of contact between the flexures.

This compaction limit study for flat flexures was simplified because bending the flexures only resulted in a single curvature profile κ_z. Therefore, one could limit the critical analysis to bending in the x–y plane and neglect the contribution of transverse components. On the other hand, folding a curved shell flexure will result in a much more complex curvature distribution. For example, the flexure center will be flattened and folded, the edge will remain at the original curvature, and everywhere in between will have varying curvature profiles based on D_{11} and D_{22} of the HSC layup. The authors are currently extending the analysis into the curved shell domain, taking inspiration from the flat flexure results.

This paper provides a general guideline to address the safe stowage limit of a flat flexure hinge that complements the authors' previous work on the deployed dynamics for the same hinge architecture [25]. When combined together, they form a flexure-based hinge design framework that can obtain the balance between flexure stiffness and compliance. This framework, for the first time, enables the designers to efficiently explore the complete parameter space and choose geometric and material combinations for a specific requirement. Once the design is close to being final, high-fidelity simulations and experimental validation should be conducted. The authors are working on experimentally demonstrating the flat flexure fabrication process and the hinge deployment characteristics [29]. This architecture is useful for cases with low panel mass, such as CubeSats or microsatellites, where the hinge stiffness requirement can be relaxed compared to compliance.

Appendix: Fittings for Elastica Results

The curve fittings extracted from the elastica analysis is presented here. The projection lengths in Fig. 7a can be approximated as:

$$\hat{L}_{x,\text{fit}} = -0.883\hat{Y}_0^3 + 0.125\hat{Y}_0^2 - 0.068\hat{Y}_0 + 0.857 \tag{A1}$$

$$\hat{L}_{y,\text{fit}}(\hat{Y}_0 < 0.457) = 1.142\hat{Y}_0^3 + 0.023\hat{Y}_0^2 + 0.305\hat{Y}_0 + 0.204 \tag{A2}$$

$$\hat{L}_{y,\text{fit}}(\hat{Y}_0 > 0.457) = \hat{Y}_0 \tag{A3}$$

Force and moments for Fig. 7b are

$$\hat{F} = \frac{5495\hat{Y}_0^2 49540\hat{Y}_0 - 33820}{\hat{Y}_0^3 + 4927\hat{Y}_0^2 - 1153\hat{Y}_0 - 3397} \tag{A4}$$

$$\hat{M} = \frac{6853\hat{Y}_0^2 7079\hat{Y}_0 - 4796}{\hat{Y}_0^3 + 3724\hat{Y}_0^2 - 2677\hat{Y}_0 - 1501} \tag{A5}$$

Maximum curvature profile for Fig. 8b are

$$G(\hat{Y}_0 < 0.6366) = 0.3905\hat{Y}_0^2 - 6.176\hat{Y}_0 + 5.348 \tag{A6}$$

$$G(\hat{Y}_0 > 0.6366) = \frac{-95.44\hat{Y}_0^2 + 170\hat{Y}_0 - 57.59}{\hat{Y}_0^3 - 1.47\hat{Y}_0^2 - 20.99\hat{Y}_0 + 21.52} \tag{A7}$$

Acknowledgments

The University of Colorado team acknowledges the Jet Propulsion Laboratory Strategic University Research Partnership for funding this project. Part of the research was carried out at the Jet Propulsion Laboratory, California Institute of Technology, under a contract with NASA (contract number 80NM0018D0004).

References

[1] Chai, T., and Tan, C., "Review on Deployable Structure," *IOP Conference Series: Earth and Environmental Science*, Vol. 220, No. 1, 2019, Paper 012034. https://doi.org/10.1088/1755-1315/220/1/012034

[2] Miura, K., and Pellegrino, S., *Forms and Concepts for Lightweight Structures*, Cambridge Univ. Press, Cambridge, England, U.K., 2020. https://doi.org/10.1017/9781139048569

[3] Pellegrino, S., Kebadze, E., Lefort, T., and Watt, A., *Low-Cost Hinge for Deployable Structures*, Univ. of Cambridge, Dept. of Engineering, Cambridge, England, U.K., 2002.

[4] Fernandez, J. M., "Advanced Deployable Shell-Based Composite Booms for Small Satellite Structural Applications Including Solar Sails," *4th International Solar Sailing Symposium*, Kyoto, Japan, 2017.

[5] Mallikarachchi, H., and Pellegrino, S., "Quasi-Static Folding and Deployment of Ultrathin Composite Tape-Spring Hinges," *Journal of Spacecraft and Rockets*, Vol. 48, No. 1, 2011, pp. 187–198. https://doi.org/10.2514/1.47321

[6] Echter, M. A., Gillmer, S. R., Silver, M. J., Reid, B. M., and Martinez, R. E., "A Multifunctional High Strain Composite (HSC) Hinge for Deployable In-Space Optomechanics," *Smart Materials and Structures*, Vol. 29, No. 10, 2020, Paper 105010. https://doi.org/10.1088/1361-665X/abad4d

[7] Soykasap, Ö., Pellegrino, S., Howard, P., and Notter, M., "Folding Large Antenna Tape Spring," *Journal of Spacecraft and Rockets*, Vol. 45, No. 3, 2008, pp. 560–567. https://doi.org/10.2514/1.28421

[8] Santiago-Prowald, J., and Baier, H., "Advances in Deployable Structures and Surfaces for Large Apertures in Space," *CEAS Space Journal*, Vol. 5, Dec. 2013, pp. 89–115. https://doi.org/10.1007/s12567-013-0048-3

[9] Sauder, J. F., Arya, M., Chahat, N., Thiel, E., Dunphy, S., Shi, M., Agnes, G., and Cwik, T., "Deployment Mechanisms for High Packing Efficiency One-Meter Reflectarray Antenna (OMERA)," *AIAA Scitech 2019 Forum*, AIAA Paper 2019-0755, 2019. https://doi.org/10.2514/6.2019-0755

[10] Yee, J., and Pellegrino, S., "Composite Tube Hinges," *Journal of Aerospace Engineering*, Vol. 18, No. 4, 2005, pp. 224–231. https://doi.org/10.1061/(ASCE)0893-1321(2005)18:4(224)

[11] Wu, Y., and Zhou, Z., "Design Calculations for Flexure Hinges," *Review of Scientific Instruments*, Vol. 73, No. 8, 2002, pp. 3101–3106. https://doi.org/10.1063/1.1494855

[12] Schotborgh, W. O., Kokkeler, F. G., Tragter, H., and van Houten, F. J., "Dimensionless Design Graphs for Flexure Elements and a Comparison Between Three Flexure Elements," *Precision Engineering*, Vol. 29, No. 1, 2005, pp. 41–47. https://doi.org/10.1016/j.precisioneng.2004.04.003

[13] Tian, Y., Shirinzadeh, B., Zhang, D., and Zhong, Y., "Three Flexure Hinges for Compliant Mechanism Designs Based on Dimensionless Graph Analysis," *Precision Engineering*, Vol. 34, No. 1, 2010, pp. 92–100. https://doi.org/10.1016/j.precisioneng.2009.03.004

[14] Seffen, K., and Pellegrino, S., "Deployment Dynamics of Tape Springs," *Proceedings of the Royal Society of London. Series A: Mathematical, Physical and Engineering Sciences*, Vol. 455, No. 1983, 1999, pp. 1003–1048. https://doi.org/10.1098/rspa.1999.0347

[15] Soykasap, Ö., "Analysis of Tape Spring Hinges," *International Journal of Mechanical Sciences*, Vol. 49, No. 7, 2007, pp. 853–860. https://doi.org/10.1016/j.ijmecsci.2006.11.013

[16] Kwok, K., and Pellegrino, S., "Folding, Stowage, and Deployment of Viscoelastic Tape Springs," *AIAA Journal*, Vol. 51, No. 8, 2013, pp. 1908–1918. https://doi.org/10.2514/1.J052269

[17] Mallikarachchi, H., and Pellegrino, S., "Deployment Dynamics of Ultrathin Composite Booms with Tape-Spring Hinges," *Journal of Spacecraft and Rockets*, Vol. 51, No. 2, 2014, pp. 604–613. https://doi.org/10.2514/1.A32401

[18] Fulton, J., and Schaub, H., "Deployment Dynamics Analysis of an Origami-Folded Spacecraft Structure with Elastic Hinges," *Journal of Spacecraft and Rockets*, Vol. 59, No. 2, 2022, pp. 401–420. https://doi.org/10.2514/1.A34938

[19] Kim, K.-W., and Park, Y., "Systematic Design of Tape Spring Hinges for Solar Array by Optimization Method Considering Deployment Performances," *Aerospace Science and Technology*, Vol. 46, Oct. 2015, pp. 124–136. https://doi.org/10.1016/j.ast.2015.06.013

[20] Yang, H., Liu, R., Wang, Y., Deng, Z., and Guo, H., "Experiment and Multiobjective Optimization Design of Tape-Spring Hinges," *Structural and Multidisciplinary Optimization*, Vol. 51, June 2015, pp. 1373–1384. https://doi.org/10.1007/s00158-014-1205-9

[21] Ye, H., Zhang, Y., Yang, Q., Xiao, Y., Grandhi, R. V., and Fischer, C. C., "Optimal Design of a Three Tape-Spring Hinge Deployable Space Structure Using an Experimentally Validated Physics-Based Model," *Structural and Multidisciplinary Optimization*, Vol. 56, Nov. 2017, pp. 973–989. https://doi.org/10.1007/s00158-017-1810-5

[22] Oberst, S., Tuttle, S., Griffin, D., Lambert, A., and Boyce, R., "Experimental Validation of Tape Springs to be Used as Thin-Walled Space Structures," *Journal of Sound and Vibration*, Vol. 419, April 2018, pp. 558–570. https://doi.org/10.1016/j.jsv.2018.01.014

[23] Ye, H., Zhang, Y., Yang, Q., and Zhang, B., "Quasi-Static Analysis and Multi-Objective Optimization for Tape Spring Hinge," *Structural and Multidisciplinary Optimization*, Vol. 60, Dec. 2019, pp. 2417–2430. https://doi.org/10.1007/s00158-019-02331-6

[24] Piovesan, D., Zaccariotto, M., Bettanini, C., Pertile, M., and Debei, S., "Design and Validation of a Carbon-Fiber Collapsible Hinge for Space Applications: A Deployable Boom," *Journal of Mechanisms and Robotics*, Vol. 8, No. 3, 2016, Paper 031007. https://doi.org/10.1115/1.4032271

[25] Dharmadasa, B. Y., Mejia-Ariza, J., Sauder, J., Focardi, P., Bradford, S. C., Arya, M., and López Jiménez, F., "Free Vibration of a Panel Supported by a Shear Compliant Two-Flexure Hinge," *AIAA Journal*, Vol. 62, No. 3, 2024, pp. 1205–1217. https://doi.org/10.2514/1.J063165

[26] Dharmadasa, B. Y., Blesinger, S., Arya, M., Mejia-Ariza, J., Sauder, J. F., Focardi, P., Bradford, S. C., and Jimenez, F. L., "A Closed-Form Formulation to Estimate the Natural Frequency of Tape Spring Hinges," *AIAA SCITECH 2024 Forum*, AIAA Paper 2024-1262, 2024. https://doi.org/10.2514/6.2024-1262

[27] Chahat, N., Arya, M., Sauder, J., Thiel, E., Zhou, M., and Cwik, T., "One Meter Reflectarray Antenna: OMERA," *CubeSat Antenna Design*, IEEE Press, New Jersey, 2020, pp. 139–162. https://doi.org/10.1002/9781119692720.ch4

[28] Levien, R., "The Elastica: A Mathematical History," *Electrical Engineering and Computer Sciences University of California at Berkeley*, Vol. 70, TR UCB/EECS-2008-103, 2008, http://www2.eecs.berkeley.edu/Pubs/TechRpts/2008/EECS-2008-103.html.

[29] Dharmadasa, B. Y., López Jiménez, F., Arya, M., Mejia-Ariza, J., Sauder, J. F., Focardi, P., and Bradford, S. C., "Design and Fabrication of a High Strain Composite Flexure for CubeSat Reflectarrays," *AIAA SCITECH 2022 Forum*, AIAA Paper 2023-0581, 2023. https://doi.org/10.2514/6.2023-0581

K. Wang
Associate Editor